HIGH POWER LASER
SCIENCE AND ENGINEERING

RESEARCH ARTICLE

High-repetition-rate source of nanosecond duration kA-current pulses driven by relativistic laser pulses

Michael Ehret [1], Jakub Cikhardt [2], Philip Wykeham Bradford [3], Iuliana-Mariana Vladisavlevici[1],
Tomas Burian[4], Diego de Luis[1], Jose Luis Henares[1], Rubén Hernández Martín[1], Jon Imanol Apiñaniz[1],
Roberto Lera[1], José Antonio Pérez-Hernández [1], João Jorge Santos[3], and Giancarlo Gatti[1]

[1] *Centro de Láseres Pulsados (CLPU), Villamayor, Spain*

[2] *Czech Technical University in Prague, Faculty of Electrical Engineering, Prague, Czech Republic*

[3] *Univ. Bordeaux-CNRS-CEA, Centre Lasers Intenses et Applications (CELIA), UMR 5107, Talence, France*

[4] *Department of Radiation and Chemical Physics, FZU-Institute of Physics of the Czech Academy of Sciences, Prague, Czech Republic*

Abstract
We report the first high-repetition-rate generation and simultaneous characterization of nanosecond-scale return currents
of kA-magnitude issued by the polarization of a target irradiated with a PW-class high-repetition-rate titanium:sapphire
laser system at relativistic intensities. We present experimental results obtained with the VEGA-3 laser at intensities from
5×10^{18} to 1.3×10^{20} W cm^{-2}. A non-invasive inductive return-current monitor is adopted to measure the derivative of
return currents of the order of kA ns^{-1} and analysis methodology is developed to derive return currents. We compare
the current for copper, aluminium and Kapton targets at different laser energies. The data show the stable production of
current peaks and clear prospects for the tailoring of the pulse shape, which is promising for future applications in high-
energy-density science, for example, electromagnetic interference stress tests, high-voltage pulse response measurements
and charged particle beam lensing. We compare the target discharge of the order of hundreds of nC with theoretical
predictions and a good agreement is found.

Keywords: current pulses; electromagnetic pulse application; high-power laser; relativistic laser plasma

1. Introduction

The continuous technical and scientific improvement of lasers[1,2] has led to stable short-pulse PW-class high-repetition-rate titanium:sapphire (Ti:Sa) systems[3,4]. If these lasers are tightly focused onto matter, the relativistic interaction yields forward-acceleration of electrons[5] that in turn can trigger pulsed bright ion beams by well-known mechanisms such as target normal sheath acceleration (TNSA)[6,7], radiation pressure acceleration (RPA)[8] and others[9] that are beneficial to isotope production[10], positron emission tomography[11], ion beam microscopy[12] and particle-induced X-ray emission (PIXE)[13], as well as inertial confinement fusion[14]. The mechanisms rely on the build-up of large accelerating potentials, which are also the source of ultra-strong electromagnetic pulses (EMPs)[15]. In particular, targets attain a strong positive net-charge due to laser-accelerated electrons that are able to escape the rising

potential barrier[16]. As a result of this, kA-level discharge pulses and return currents can be produced and propagate over the target surface[17]. Interest in these effects is twofold: (i) both are sensitive to the total amount of charge that leaves the target and therefore can be used as a passive diagnostic of the laser–target interaction; and (ii) both allow one to deliver all-optically generated ns-duration kA-level current pulses that can be understood as a novel secondary source.

Note that ns-duration current pulses can also be generated by non-relativistic ns-duration laser pulses of high energy in the wide range of several A up to the MA level[18–20]. Here, the long laser pulses are issued in the single-shot regime and interact with tailor-made single-shot targets, building up a charge separation that triggers a return current to rise.

The monitoring of target discharge is an important aspect of ultrahigh intensity laser–solid interaction at high repetition rates. This paper presents an inductive current monitor as metrology for high-voltage pulses driven at high repetition rates. The measurement of return currents with inductive current monitors has been demonstrated previously in the regime of ns-driver lasers with intensities from 1×10^{14}

1

to 1×10^{16} W cm^{-2}[21]. We apply this technique to the characterization of discharge pulses driven by high-power Ti:Sa systems at relativistic intensities.

Pulses of kA-level at ns-duration pose a risk for electronic systems in the vicinity of the interaction[22,23], but they also have an application in the context of proton beam focusing[24,25] and transient magnetic field generation[17]. We demonstrate here for the first time the stable generation of discharge pulses, with a clear perspective to obtain a novel high-repetition-rate source of kA-scale current pulses for future applications, for example, in the field of electromagnetic compatibility (EMC) tests[26], radio-location[27], military technologies[28], biology[29] and medicine[30].

2. Materials and methods

The primary diagnostic used in this study was a target charging monitor (TCM) constructed based on the principles of an inductive current monitor[21]. The TCM measures the derivative of the current that streams through the device, as shown in Figure 1. The key advantage of this metrology technique is its destruction-free nature. Current pulses are excited by laser–plasma interaction on a solid-density target, transported through the TCM and can be applied after their characterization.

Current pulses that pass through the TCM device induce a magnetic field inside the cylindrical copper body, which causes an induced current to flow in a coil-shaped rod connected to an coaxial output. The calibration factor,

which relates the time-integrated voltage to the current, is $-2.0(3) \times 10^{9}$ A V^{-1} s^{-1} (see Appendix A; notation with the standard uncertainty in the last digits given in parenthesis in accordance with ISO GUM JCGM100:2008 7.2.2). For this work, current pulses are transported via RG142 coaxial cables and the circuit impedance is $Z = 50\ \Omega$. The through signal is terminated in the facility grounding. Note that cable lengths are measured with 3 ns full-width at half-maximum (FWHM) voltage pulses: the target and TCM are connected with a coaxial cable of 9.6(2) ns length, and the TCM and grounding are connected with a coaxial cable of 13.6(1) ns length. Induced signals are transported to a 2 GHz oscilloscope and acquisitions are throughout corrected for the frequency dependent attenuation of circuit elements. Circuit calibrations are done using an R&S ZNH 4 GHz vector network analyser. The effective bandwidth of the circuit is 2 GHz.

Experiments for this work are conducted at the VEGA-3 laser facility at Centro de Láseres Pulsados (CLPU) with high-power Ti:Sa laser pulses amplified to an energy E_L up to 25 J per pulse measured behind the compressor. After compression to a duration τ_L of 30 fs, the short laser pulse is transported in high-vacuum of 1×10^{-6} mbar via an $f = 2.5$ m off-axis parabola onto the target with a beam-transport efficiency of 82%. The focal spot of $d_L = 12.8(19)\ \mu$m FWHM is maintained at a constant size. The energy on target is extrapolated from calibrations recorded at low energy, and the focal spot at high energy is estimated to be the same as for low-energy measurements.
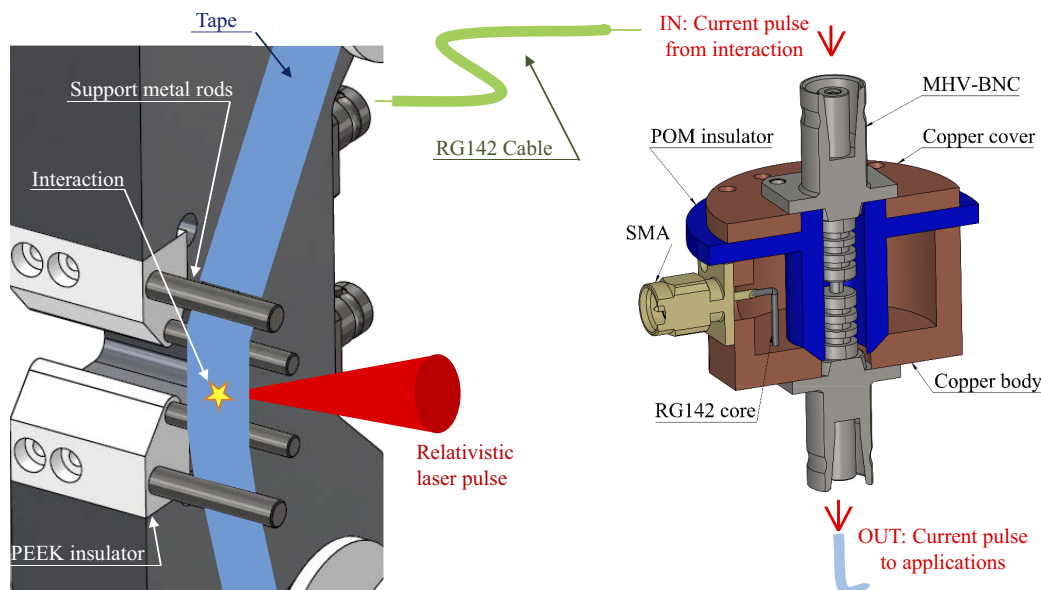

Figure 1. Tape target system (left) and cut of the target charging monitor (TCM; right). The TCM has two opposite miniature high voltage Bayonet Neill-Concelman radio-frequency (MHV-BNC) connectors with soldered pins to pass through the pulsed current issued by relativistic laser interaction in the top to the application side in the bottom. The TCM comprises a solid copper body forming a cup with a cylindrical top; both of which are later separated by dielectric material polyoxymethylene (POM). The through current induces a magnetic field enclosed in the cylinder, which causes an induced current to flow in a small squared loop formed by the core of an RG142 coaxial cable connected to an output SMA connector. The current pulse itself is issued by the discharge of the solid tape target and coupled into one of the insulated support rods of the tape, which are connected to an RG142 coaxial cable leading to the TCM via an MHV-BNC connector on the system's chassis. The other support rod is isolated from the ground.

Note the large Rayleigh length of 464(145) µm for this work, with a non-diffraction limited focal spot. For this experiment, 33.9(15)% of the energy on target is within in the first Airy disk at low power. In addition there are three hot spots aside from the focus in the first Airy ring, containing in total as much as 20(2)% of the energy on target with an average intensity of 24(2)% of the main intensity. The hot spots could not be optimized, which might be due to the age of the parabola. The main peak intensity ranges from 2×10^{19} to 1.2×10^{20} W cm^{-2} and is the reference intensity for all calculations and plots in the following. The pulse duration is measured on-shot with a second-harmonic autocorrelator system that diagnoses the faint reflection from a thin pellicle positioned between the parabola and focus.

The tape target system, TaTaS-PW[31], transported aluminium tape of 10(1) µm thickness, Kapton tape of 89(9) µm thickness, tape of 10(1) µm aluminium enforced with Kapton (Al-e-K)[31] and copper tape of 7(1) µm thickness across the laser focal plane. The tapes are 12.5 mm wide stripes. The conductive 5 mm diameter support metal rods that guide the tape are 16 mm separated. Solid-density targets are placed in the laser focus position and tilted by 12.5° with respect to the laser axis to avoid reflection back towards the laser amplifiers. As the VEGA laser pulse shows no pre-pulses capable of inducing a transparency or breakdown of the target[32], the main acceleration mechanism of charged particles is TNSA with the deployed laser and target parameters. In TNSA, a population of laser-heated forward-directed relativistic electrons escapes the target after crossing its thickness, and the successive potential dynamics and electron-refluxing lead to the formation of sheath fields that are capable of accelerating ionized surface contaminants up to several tens of MeV u^{-1}[33]. The TCM measures the return current towards the target and allows us to deduce the total target charging by relativistic electrons. Note that the tape's only connection to the ground is one of the support metal rods. The other metal rod is floating with a total conductive length of 95 mm. This forces the return current to flow through the non-floating support metal rod and successively in the core of the coaxial transmission line that incorporates the TCM. The shield of the transmission line is grounded with the chassis of the tape target system.

Numerical simulations are performed to compare experimental results to theoretical predictions. The laser-driven target discharge is simulated with ChoCoLaT-2[16] (see Appendix B) and the laser-absorption efficiency into hot electrons is studied with the particle-in-cell (PIC) code Simulating Matter Irradiated by Light at Extreme Intensities (SMILEI)[34] (see Appendix C).

3. Results and discussion

We firstly show results from a single, representative shot on an aluminium target to emphasize different aspects of the
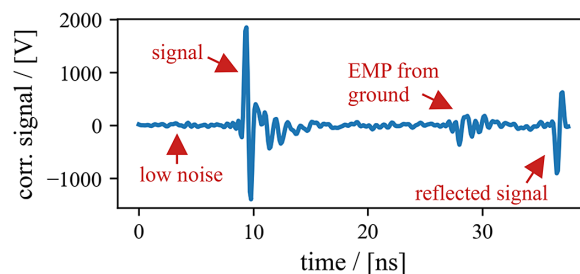

Figure 2. The circuit-corrected signal of the TCM for an aluminium target exhibits a clear positive peak for the rising edge of the positive current pulse. It is preceded by a low-noise pedestal and followed by pulses streaming from the grounding to the target: first the EMP-induced noise and second the reflection of the current pulse at the impedance mis-matched the ground. The time-base at the TCM relative to laser arrival is approximately equal to 0 ns.

platform, and secondly study the effect of changes of laser and target parameters based on single-shot data and high-repetition-rate recordings.

The inductive TCM device measures the derivative dtI_p of the pulsed current I_p streaming away from the target (see Figure 2). Here, the laser pulse at 22.5 J beam energy (after the compressor) and with a duration of 30.4(7) fs is fired onto a 10(1) µm thick aluminium target. The laser impacts on the target at zero time seen from the TCM. The spatial distance between the TCM and target is 30(1) cm to ensure that the spherically expanding vacuum bound EMP arrives at the device first. The EMP has no significant influence on the measurement, as one does not notice noise in the pedestal leading to the signal. The signal exhibits a first positive peak that detects the rising edge of the current pulse streaming through the device. This indicates a positive current pulse propagating from the target to the ground. We measure the net negative charge escaping from the target – the time between electron and ion escape is too short to be resolved. The measurement shows also a reflection of the current pulse that streams back from the imperfectly impedance matched grounding towards the target and the EMP-induced noise that couples into the transmission line when the spherically expanding EMP reaches the grounding.

After application of the instrument calibration, the temporally integrated signal is as shown in Figure 3. The peak amplitude reaches 1123(172) A. The FWHM τ_d of the narrow first peak is 400 ps. A broad second peak follows and decays slowly towards zero, which is reached after 6 ns. The first peak corresponds to the direct coupling of the discharge pulse into the transmission line to the TCM. The difference between the shortest (directly to ground) and longest way (to the opposite end of rod) from the interaction region to the exit of the grounding rod is equivalent to 100 ps at the speed of light. Capacitive effects may broaden the peak further. The second peak most likely comprises multiple reflections across the conductive tape target.

Further temporal integration of ZI_p^2 yields the transported energy E_p, and $\int I_p dt$ yields the transported charge Q_p. The
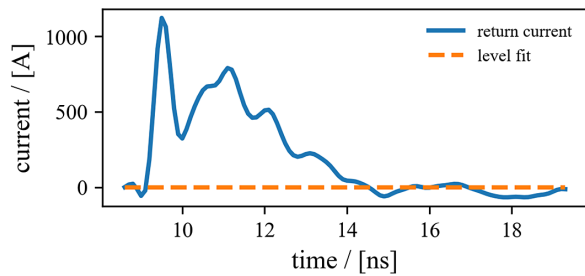
Figure 3. Current pulse (blue line) from an aluminium target retrieved by numerical integration from the derivative measured with the TCM. A first short primary peak is followed by a superposition of peaks in a broad secondary peak. The time-base relative to laser arrival is approximately equal to 0 ns. The zero-level is controlled by comparison to a fit from before to after the current pulse (orange dashed line) – here in good agreement.
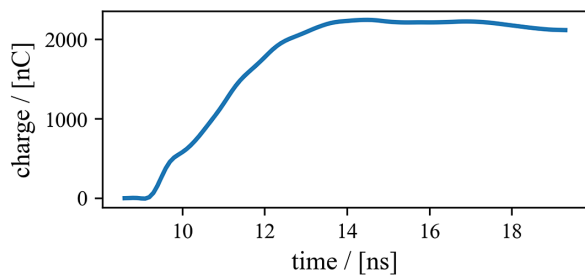

Figure 4. The transported charge from an aluminium target as obtained by numerical double-integration of the derivative measured by the TCM. The integral attains a plateau only slowly due to a slightly negative tail of the return current. The time-base relative to laser arrival is approximately equal to 0 ns.

total transported energy is 67(7) mJ. The energy conversion efficiency from laser energy on target to current pulse energy results in $\chi_T = 0.4\%$, and the energy conversion efficiency only accounting for laser energy encircled in the laser focus and relativistic-intensity hot spots is calculated as $\chi_S = 0.6\%$. The broad second peak contains a non-negligible fraction of the pulse energy in this configuration with 43(7) mJ. The temporally resolved transported charge Q_p is shown in Figure 4. The laser extracts 2.24(0.34) μC from the target. The first peak of the current accounts for less than a third of the transported charge and the slow decay of the second peak allows the integral to reach a plateau only slowly.

For control of the accuracy of the numerical integrations, the zero-level is compared to a fit of both plateaus before and after the current pulse, shown as the orange dashed line in Figure 3. Here, the zero-level is maintained.

Crucial for applications, the current pulse is reproducible over hundreds of shots and is consistent with theoretical estimates. A current of 558(116) A is obtained in 292 shots at 1 Hz for laser shots of 24.5(3) J at 33(2) fs onto copper tape of 7(1) μm thickness. The average current and its standard deviation are shown in Figure 5. The 8% stability of the current measurement indicates good shot-to-shot stability of laser and target parameters, resulting in reproducible discharge dynamics and current production.
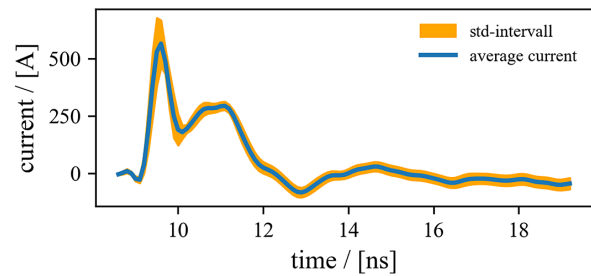

Figure 5. Average current and its standard deviation as obtained in 292 laser shots of $1.0(5) \times 10^{20}$ W cm^{-2} at 1 Hz onto copper tape. The time-base relative to laser arrival is approximately equal to 0 ns. Multiple reflections across the conductive target yield a succession of multiple peaks.

The total transported charge amounts to 713(60) nC and the current pulse energy is 11(2) mJ. The energy conversion efficiencies are lower compared to those for aluminium: $\chi_T^{Cu} = 0.05\%$ and $\chi_S^{Cu} = 0.09\%$.

ChoCoLaT-2 simulations predict 720(75) nC of target discharge when assuming 68% of the laser energy on target to be absorbed into electrons. Simulations take into account the experimental uncertainty for the pulse duration (33(2) fs), 6.8(3) J of laser energy within the first Airy disk and 4.1(3) J distributed in three non-negligible hot spots with an average intensity of 24% of the main intensity. The absorption efficiency into electrons is consistent with PIC simulations (see Appendix C). Such high values have been reported[35], depending on the presence of pre-plasma. If, however, the 2D PIC simulations should overestimate the absorption or no pre-plasma is present, a typical[36,37] absorption of 50% would still lead to an agreement with overlapping uncertainty intervals.

A comparison of the metallic targets above to a dielectric target reveals the likely influence of target reflections and shows how we can produce single-peak current pulses. A current of 597(153) A is obtained in 100 shots at 0.5 Hz for laser shots of 22.9(2) J at 33(1) fs onto Kapton tape of 89(9) μm thickness. The current evolution (averaged over multiple shots) is shown in Figure 6. The peak of 960 ps FWHM transports an average of 934(190) nC and has an energy of 13(4) mJ. The energy conversion efficiencies are comparable to those for copper: $\chi_T^K = 0.06\%$ and $\chi_S^K = 0.1\%$. In comparison to metallic targets, the primary peak is broadened due to reduced conductivity and secondary peaks from reflections are missing. Multi-peak structures are indeed not expected to appear as reflections on tape ends do not occur, and reflections on other grounding stalks do not reach the signal transmission line with noticeable amplitude after the shot due to the low conductivity. Fewer reflections on the target may contribute towards the reduced EMP emission that is generally observed for dielectric targets[15].

Compared to the measurement for Kapton targets, simulations with ChoCoLaT-2 indicate a 10× lower current due to the dielectric nature of the material, but the code is not

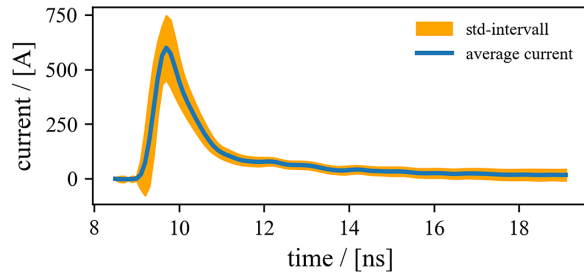**Figure 6.** Average current and its standard deviation as obtained in 100 laser shots of $1.0(5) \times 10^{20}$ W cm^{-2} at 0.5 Hz onto Kapton tape. The dielectric target allows one to produce single pulses. The time-base relative to laser arrival is approximately equal to 0 ns.

benchmarked for dielectric target materials where simulations do not consider the pre-plasma and pre-ionization of the target material, which will increase conductivity and lower the target potential, and therefore increase the total target discharge.

It becomes clear that the current evolution and the amount of total charge vary considerably under variation of the target parameters. For a further parametric study on the variation of laser intensity, shots on aluminium tape, Kapton tape, tape of aluminium enforced with Kapton (Al-e-K)[31] and copper tape are compared in Figure 7(a). Most charge is ejected from aluminium targets, followed by copper and Kapton. Shots on aluminium reveal a monotonic relation between target discharge and intensity from 2.0×10^{19} to 1.2×10^{20} W cm^{-2}. The large spread within the sets of data is due to the simultaneous variation of laser pulse duration and energy: when fixing the laser pulse energy, the ejected charge reaches a plateau towards shorter laser pulse duration, consistent with the available literature[16]. The platform allows for the production of tunable current pulses.

Figure 7(b) shows the amount of total charge under variation of the laser energy E_L for single-shot data obtained at best laser compression with a laser pulse duration ranging from 29 to 35 fs. The total target discharge can be modelled as a function of the hot electron temperature T_e of the laser-accelerated relativistic electron population as $Q_p = A_i \cdot T_e$. Values for the tape dependent constant A_i are given in Table 1, which result from the fits shown in Figure 7(b). Here T_e is presumed to follow ponderomotive scaling[39]. One notes the good agreement of this square-root relation between laser energy and target discharge, which confirms previous work in the ponderomotive regime[16], and renders it possible to extrapolate the results to future experiments in similar conditions.

The thermalizing electron cloud is foundational to TNSA, which motivates an investigation of the relation between the return current and the sheath field based on properties of TNSA ions. The cut-off energy for TNSA-accelerated protons is obtained from a Thomson parabola ion spectrometer[40] positioned towards the nominal target normal direction; see Figure 7(c) for the same shots as in Figure 7(b).
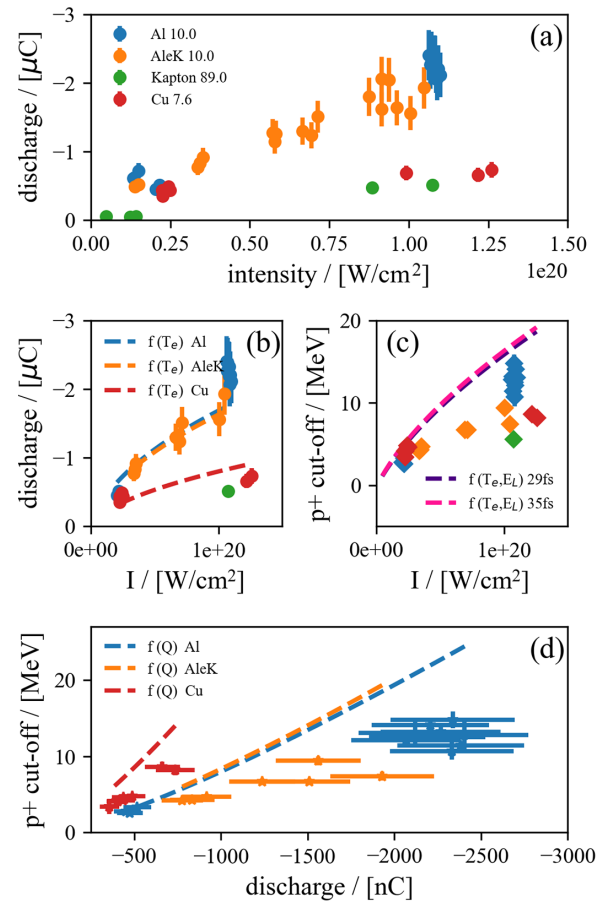

Figure 7. (a) Total charge measured under variation of laser pulse duration, energy and the target material. (b)–(d) Select data obtained at best laser compression: (b) comparison with a semi-empirical model to derive the total charge from T_e and a material constant; (c) spectral cut-off energies for protons in the target normal direction compared to available modelling[38]; (d) the relation between target charge and proton cut-off energy.

Table 1. Comparison of the proportionality factor A_i in the scaling model $Q_p = A_i \cdot T_e$ for aluminium tape (Al), Kapton-reinforced aluminium tape (Al-e-K) and copper tape (Cu).

Tape	Al	Al-e-K	Cu
$A_i / [\text{nC MeV}^{-1}]$	538(45)	520(16)	256(26)

Figure 7(c) shows a proportionality between the proton cut-off energy and the total amount of charge.

The distribution of accelerated ions was successfully modelled in the regime relevant to this work[38], with the maximum energy of ions with charge Z scaling as $E_i^{\max} = Z \cdot T_e \cdot (P/T_e - 1)$, where P is a monotonically rising function of the maximum electron energy in the electron cloud. The ratio P/T_e simplifies to $P/T_e \approx 4.8 + 0.8 \cdot \ln\left(E_L^{[\text{J}]}\right)$ for laser energies larger than several J[38]. The dashed lines in Figure 7(c) show the model predictions for each intensity at 29 and 35 fs. One notes that the model predictions are an upper bound for the measured proton cut-off energies. The model does not take into account that the material properties of targets and discrepancies might be due to differences in

Table 2. Comparison of current pulses from shots on aluminium tape (Al), Kapton-reinforced aluminium tape (Al-e-K), Kapton tape (Kapton) and copper tape (Cu). Laser energy is measured after the compressor, N denotes the number of shots of the sequence and χ_T is the ratio of energy confined in the current pulse to laser energy on target.

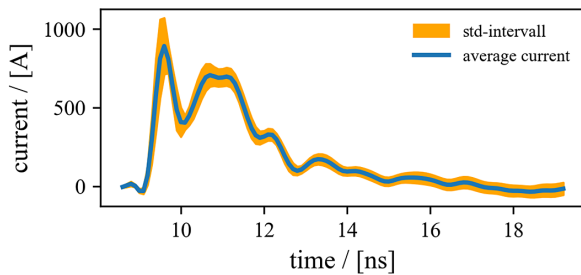| Laser pulse				Target			Current pulse			
Energy	Duration	Rate	N	Tape	Material	Thickness	Peak	Charge	Energy	χ_T
22.0(3) J	33(2) fs	0.5 Hz	87	Al	Al	10(1) µm	982(185) A	2.2(2) µC	58(9) mJ	0.32%
21.9(3) J	37(4) fs	1 Hz	25	Al-e-K	Al	10(1) µm	809(210) A	2.1(3) µC	45(8) mJ	0.25%
22.9(2) J	33(2) fs	0.5 Hz	100	Kapton	Kapton	89(9) µm	597(153) A	0.93(19) µC	13(4) mJ	0.06%
24.5(3) J	33(2) fs	1 Hz	292	Cu	Cu	7(1) µm	558(116) A	0.71(6) µC	11(2) mJ	0.05%

Figure 8. Average current and its standard deviation as obtained in 25 laser shots of $0.8(4) \times 10^{20}$ W cm^{-2} at 1 Hz onto Al-e-K tape. The time-base relative to laser arrival is approximately equal to 0 ns.

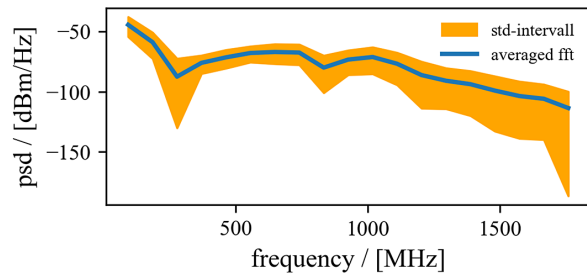**Figure 9.** Average power spectrum density and its standard deviation as obtained in 25 laser shots of $0.8(4) \times 10^{20}$ W cm^{-2} at 1 Hz onto Al-e-K tape. The time-base relative to laser arrival is approximately equal to 0 ns.

the accelerating potential induced by the respective size of the electron cloud that is influenced by electron scattering. Further, the model might be not applicable to Kapton targets as they are not conductive.

In order to relate target discharge and proton cut-off energy, both models are combined to deduce T_e from the total charge and calculate the proton cut-off energy accordingly. Respective predictions for each material are compared to the data as dashed lines in Figure 7(d). The agreement is fair when we consider the simplicity of the underlying models. There is a systematic overestimation by a factor approximately equal to 1.8.

Note the geometry of the Al-e-K tape: two 5 mm wide strips of 89 µm thick Kapton are glued on top of the aluminium tape at both its edges on the side facing the support metal rods. This Kapton reinforcement of aluminium is at mm-distance from the interaction zone, so it does not change the total amount of ejected charge (consistent with the experimental measurements in Figure 7(a)). However, in Figure 7(c) the proton cut-off energy in the spectrometer appears to be lower for Al-e-K tape than for aluminium tape. A tilt of the Al-e-K tape could have caused the proton cone to be not perfectly aligned towards the detector, resulting in a drop of detected maximum energy (as the highest energies have the smallest divergence in the TNSA scheme[9]). Such tilts are readily explained by tensions in the multi-layer structure. The temporal shape of the current pulse can, however, be influenced by the Kapton enforcement for Al-e-K tape (see Figure 8 (compared to Figure 3)). The first peak is lower, which is consistent with the reduced coupling to the grounding due to the presence of Kapton at the tape edges.

As a result, the secondary peaks in the tail are elevated for reasons of more charge in reflections.

The characteristic parameters for all shot sequences are compared in Table 2. Current pulses from aluminium tape and reinforced aluminium tape are in a good agreement. Results for aluminium tapes exhibit higher current amplitudes when compared to copper targets due to a larger target discharge.

The bandwidth of the current pulse is large and allows for applications that require broadband pulses[27] (see Figure 9). Such pulses can be applied to steering antenna arrays or impulse radiating antennas to emit high power levels, that is, in ground and subsurface radars for finding, recognition and reconstruction of moving objects.

4. Conclusions

We report the first generation and characterization of short-pulsed kA-scale currents induced by high-power relativistic laser interaction at a high repetition rate. The pulses with several 100 ps FWHM show less than 10% stability in amplitude and a high energy conversion efficiency up to the order of 1% from laser energy to pulse energy. Although the conversion efficiency of laser energy to electrical current can be one order of magnitude higher for kJ-class (ns-duration) laser pulses, fs-duration systems have the advantage of a high repetition rate and (potentially) more stable interaction conditions. Optimization of the energy conversion efficiency in relativistic interactions will be possible by optimizing the target discharge based on existing theoretical models[16], as the experimental data appear to agree well with simulations.

Another advantage of the presented scheme is that it allows carrying the electrical impulse by cable out of the interaction chamber, whereas non-relativistically generated current dynamics clings to the close vicinity of the laser–target interaction point. Current pulses can be tailored by modifying the target: experimental data show that the return current to metallic targets is broadened due to reflections across the target, whereas the use of dielectric targets removes those reflections, leading to the generation of an overall shorter pulse peak.

The highest charge of 2.2(2) µC is produced with aluminium targets, followed by Kapton targets with 0.93(19) µC and copper targets with 0.71(6) µC.

A direct application of such pulses can be the inductive generation of pulsed strong magnetic fields in small volumes. The pulse fills a solenoid if $\tau_d \times c = 2\pi \times r_c \times N_c$, with the speed of light c, the radius of the coil r_c and N_c revolutions. Then the induced magnetic field in the coil centre attains $B_c = \mu_0 I_d c \tau_d / 2\pi r_c l_c$, with vacuum permeability μ_0 and the solenoid length l_c. The measured pulse of 1.1 kA amplitude and 400 ps FWHM is apt for the generation of 11 T when using 1 mm diameter coils of 5 mm length, corresponding to 40 revolutions. Such magnetic fields can be used for the tailoring of MeV u^{-1} ions[24,25], that is, laser-accelerated ion beams. They are also relevant for the magnetization of secondary samples[41–43] if further temporally stretched, that is, as seed fields in the context of magnetized implosions towards nuclear fusion.

Pulses of 1.1 kA in the 50 Ω circuit correspond to pulsed voltages of 55 kV that are, for example applicable to unipolar nanosecond-pulse dielectric barrier discharge for producing non-thermal plasma at atmospheric pressure[44] or the research of effects of ns and sub-ns pulses on biological cells[45–48].

Appendices

A. TCM calibration

A pulsed high-voltage supply (500 ps FWHM) is used for the calibration of the TCM. The voltage supply is plugged to the top of the TCM. The through signal and the signal from the induced current are recorded on an oscilloscope of 20 GHz bandwidth using calibrated coaxial cables in a 50 Ω circuit (see Figure 10). The current of the pulse can be naturally derived from the impedance of the circuit.

The induced signal is integrated numerically to derive the calibration factor between the pulsed current and the measured current (see Figure 11). The numerical integration may lead to what one observes as a change of the zero-level from before to after the peak. It is corrected for by fitting a zero-level with a linear regression. The difference between measurement and fit is fully taken into account in the following uncertainty estimates.
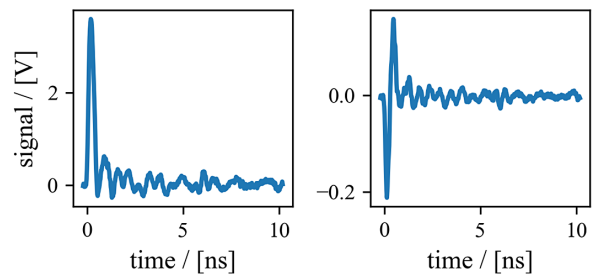

Figure 10. Through signal (left) and induced signal (right) corrected for attenuation of the respective circuit after the TCM.
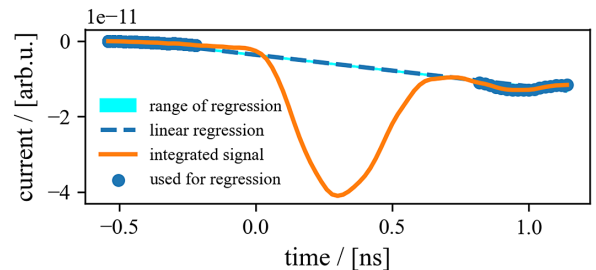

Figure 11. The integrated induced signal (orange line) shows a small offset after the pulse, which might be due to numerical errors. Plateau regions before and after the peak are selected (blue dots) to fit a correction (dashed blue line) with respective uncertainty (cyan area).
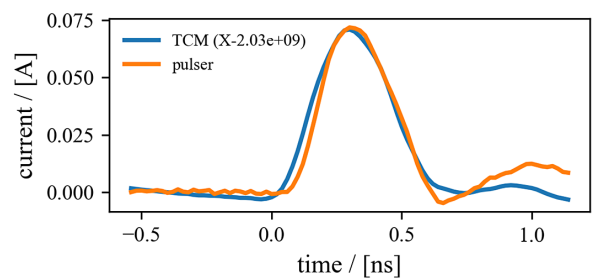

Figure 12. The integrated induced signal (blue line) is scaled to the pulsed through current (orange line) to obtain the calibration factor in units of A V^{-1} s^{-1}.

The calibration factor, which relates the integrated induced measurement in units of volt to the pulsed through current, is obtained by fitting the base-corrected integrated induced signal to the through current (see Figure 12). One obtains a calibration factor of $-2.0349(3117) \times 10^9$ A V^{-1} s^{-1}.

B. Discharge simulations

The target discharge dynamics is studied using a detailed model of target charging in short laser pulse interactions[16] that predicts the expected discharge due to laser-heated relativistic electrons on a thin disk target. The initial electron distribution is based on laser parameters, with the temperature proportional to the intensity and the amount of charge proportional to the laser energy. The model takes into account the collisional cooling of electrons within cold solid-density targets. Electrons are prevented from escaping the

target by the target electric potential, which depends both on the target capacitance and the temperature of the plasma sheath at the target surface. The result of this calculations is the total amount of target charge, which can be compared to integrated measurements of the return current.

The energy and time-dependent hot electron distribution function $f(E,t)$ describes electrons inside the target and evolves according to the following:

$$\partial_t f(E,t) = \frac{h_L(E)\Theta(\tau_L - t)}{\tau_L} - \frac{f(E,t)}{\tau_{ee}(E)} - g(E,t), \qquad (1)$$

$$h_L(E) \overset{!}{=} \frac{N_0}{T_0}\exp(-E/T_0), \qquad (2)$$

$$N_0 \overset{!}{=} \int f(E,0)\,\mathrm{d}E, \qquad (3)$$

where $h_L(E)$ is a constant exponential source of hot electrons, $\Theta(t)$ is the Heaviside function limiting electron heating to the laser duration, $\tau_{ee}(E)$ is the energy-dependent cooling time and $g(E,t)$ is the rate of electron ejection from the target. The initial hot electron temperature T_0 depends on the laser wavelength and pulse intensity[39,49,50], and N_0 is renormalized to the energy balance $N_0 T_0 = \eta E_L$ between the total energy of hot electrons in the target and the absorbed laser energy. Simulations require the conversion efficiency η of laser energy to energy in the hot electron distribution, which is obtained by PIC simulations for this work (see Appendix C).

The hot electron cooling time depends on target material properties, such as mass density ρ_t, mass number A_t, atomic number Z_t, and hot electron energy distribution that allows one to calculate average speed $\langle v\rangle_e$ and energy $\langle E\rangle_e$. Its meticulous calculation is demonstrated in Ref. [51] with an emphasis on cases relevant to this work.

With slight modifications to the source code, we can account for a second population of electrons produced by laser intensity hot spots in and around the main focus. A section is added to construct an electron distribution based on the hot spot energy and intensity, which then is added on top of the main electron distribution function.

C. PIC simulations

The absorption of laser pulse energy into hot electron energy is studied for the case of shots on the copper target in a typical range of pre-plasma scale lengths. The absorption results are 61% for 1 μm pre-plasma and 78% for 3 μm pre-plasma. This range covers the absorption efficiencies required to reproduce experimental target charging by discharge simulations.

The 2D PIC simulation setup consists of a solid copper target irradiated by the VEGA-3 laser system under an incidence angle of 12.5°. The laser is linearly polarized and has the following characteristics: a wavelength λ of 800 nm,

a peak intensity of 7.5×10^{19} W cm^{-2} (corresponding to a normalized field amplitude $a_0 = 5.9$), a pulse duration of 33 fs FWHM and a transverse waist of 13 μm. The copper target is considered fully ionized, having a density $100 n_c$ and a thickness of 7 μm. The plasma density scale lengths are considered to be 1 and 3 μm for the two distinct simulations, having an exponential profile over a length of 20 μm and being ablated from the initial target thickness. The transverse width of the target is 40 μm. At the rear side of the target we considered a thin layer of neutral protons of 70 nm thickness and $10 n_c$ density to simulate target contaminants. The simulation box is 80 μm in the longitudinal direction and 40 μm in the transverse direction. The cell length is $\mathrm{d}x = \mathrm{d}y = 12.5$ nm and the number of particles per cell is 20 for each species. The particles are deleted while crossing the domain boundaries and the fields are absorbed. The simulations were performed with SMILEI[34] on the cluster Supercomputación Castilla y León (SCAYLE)[52].

been carried out within the framework of the EUROfusion Consortium, funded by the European Union via the Euratom Research and Training Programme (grant agreement No. 101052200 – EUROfusion). The views and opinions expressed are however those of the author(s) only and do not necessarily reflect those of the European Union or the European Commission. Neither the European Union nor the European Commission can be held responsible for them. The involved teams have operated within the framework of the Enabling Research Projects: AWP17-ENR-IFE-CEA-02 *Towards a universal Stark-Zeeman code for spectroscopic diagnostics and for integration in transport codes* and AWP21-ENR-IFE.01.CEA *Advancing shock ignition for direct-drive inertial fusion*.

Data availability statement

The raw data and numerical methods that support the findings of this study are available from the corresponding author upon reasonable request.

References

1. T. H. Maiman, Nature **187**, 493 (1966).
2. M. DiDomenico, J. E. Geusic, H. M. Marcos, and R. G. Smith, Appl. Phys. Lett. **8**, 180 (1966).
3. P. Maine, D. Strickland, P. Bado, M. Pessot, and G. Mourou, IEEE J. Quantum Electron. **24**, 398 (1988).
4. M. Aoyama, K. Yamakawa, Y. Akahane, J. Ma, N. Inoue, H. Ueda, and H. Kiriyama, Opt. Lett. **28**, 1594 (2003).
5. T. Tajima and V. Malka, Plasma Phys. Control. Fusion **62**, 034004 (2012).
6. R. A. Snavely, M. H. Key, S. P. Hatchett, T. E. Cowan, M. Roth, T. W. Phillips, M. A. Stoyer, E. A. Henry, T. C. Sangster, M. S. Singh, S. C. Wilks, A. MacKinnon, A. Offenberger, D. M. Pennington, K. Yasuike, A. B. Langdon, B. F. Lasinski, J. Johnson, M. D. Perry, and E. M. Campbell, Phys. Rev. Lett. **85**, 14 (2000).
7. S. C. Wilks, A. B. Langdon, T. E. Cowan, M. Roth, M. Singh, S. Hatchett, M. H. Key, D. Pennington, A. MacKinnon, and R. A. Snavely, Phys. Plasmas **8**, 542 (2001).
8. T. Esirkepov, M. Borghesi, S. V. Bulanov, G. Mourou, and T. Tajima, Phys. Rev. Lett. **92**, 175003 (2004).
9. M. Borghesi, in *Laser-Driven Sources of High Energy Particles and Radiation*, Springer Proceedings in Physics (Springer, 2019), p. 143.
10. K. Nemoto, A. Maksimchuk, S. Banerjee, K. Flippo, G. Mourou, D. Umstadter, and V. Y. Bychenkov, Appl. Phys. Lett. **78**, 595 (2001).
11. M. I. K. Santala, M. Zepf, F. N. Beg, E. L. Clark, A. E. Dangor, K. Krushelnick, M. Tatarakis, I. Watts, K. W. D. Ledingham, T. McCanny, I. Spencer, A. C. Machacek, R. Allott, R. J. Clarke, and P. A. Norreys, Appl. Phys. Lett. **78**, 19 (2001).
12. F. E. Merrill, A. A. Golubev, F. G. Mariam, V. I. Turtikov, and D. Varentsov, AIP Conf. Proc. **1195**, 667 (2009).
13. F. Mirani, A. Maffini, F. Casamichiela, A. Pazzaglia, A. Formenti, D. Dellasega, V. Russo, D. Vavassori, D. Bortot, M. Huault, G. Zeraouli, V. Ospina, S. Malko, J. I. Apiñaniz, J. A. Pérez-Hernández, D. DeLuis, G. Gatti, L. Volpe, A. Pola, and M. Passon, Sci. Adv. **7**, 3 (2021).
14. M. Roth, T. E. Cowan, M. H. Key, S. P. Hatchett, C. Brown, W. Fountain, J. Johnson, D. M. Pennington, R. A. Snavely, S. C. Wilks, K. Yasuike, H. Ruhl, F. Pegoraro, S. V. Bulanov, E. M. Campbell, M. D. Perry, and H. Powell, Phys. Rev. Lett. **86**, 436 (2001).
15. F. Consoli, V. T. Tikhonchuk, M. Bardon, P. W. Bradford, D. C. Carroll, J. Cikhardt, M. Cipriani, R. J. Clarke, T. E. Cowan, C. N. Danson, R. De Angelis, M. De Marco, J.-L. Dubois, B. Etchessahar, A. Laso Garcia, D. I. Hillier, A. Honsa, W. Jiang, V. Kmetik, J. Krasa, Y. Li, F. Lubrano, P. McKenna, J. Metzkes-Ng, A. Poyé, I. Prencipe, P. Raczka, R. A. Smith, R. Vrana, N. C. Woolsey, E. Zemaityte, Y. Zhang, Z. Zhang, B. Zielbauer, and D. Neely, High Power Laser Sci. Eng. **8**, e22 (2020).
16. A. Poyé, S. Hulin, J. Ribolzi, M. Bailly-Grandvaux, F. Lubrano-Lavaderci, M. Bardon, D. Raffestin, J. J. Santos, and V. Tikhonchuk, Phys. Rev. E **98**, 033201 (2018).
17. M. Ehret, M. Bailly-Grandvaux, P. Korneev, J. I. Apinaniz, C. Brabetz, A. Morace, P. W. Bradford, E. d'Humieres, G. Schaumann, V. Bagnoud, S. Malko, K. Matveevskii, M. Roth, L. Volpe, N. C. Woolsey, and J. J. Santos, Phys. Plasmas **30**, 013105 (2023).
18. S. Fujioka, Z. Zhang, K. Ishihara, K. Shigemori, Y. Hironaka, T. Johzaki, A. Sunahara, N. Yamamoto, H. Nakashima, T. Watanabe, H. Shiraga, H. Nishimura, and H. Azechi, Sci. Rep. **3**, 1170 (2013).
19. J. J. Santos, M. Bailly-Grandvaux, M. Ehret, A. V. Arefiev, D. Batani, F. N. Beg, A. Calisti, S. Ferri, R. Florido, P. Forestier-Colleoni, S. Fujioka, M. A. Gigosos, L. Giuffrida, L. Gremillet, J. J. Honrubia, S. Kojima, P. Korneev, K. F. F. Law, J.-R. Marquès, A. Morace, C. Mossé, O. Peyrusse, S. Rose, M. Roth, S. Sakata, G. Schaumann, F. Suzuki-Vidal, V. T. Tikhonchuk, T. Toncian, N. Woolsey, and Z. Zhang, Phys. Plasmas **25**, 056705 (2018).
20. G. J. Williams, S. Patankar, D. A. Mariscal, V. T. Tikhonchuk, J. D. Bude, C. W. Carr, C. Goyon, M. A. Norton, B. B. Pollock, A. M. Rubenchik, G. F. Swadling, E. R. Tubman, and J. D. Moody, J. Appl. Phys. **127**, 083302 (2020).
21. J. Cikhardt, J. Krása, M. De Marco, M. Pfeifer, A. Velyhan, E. Krouský, B. Cikhardtová, D. Klír, K. Řezáč, J. Ullschmied, J. Skála, P. Kubeš, and J. Kravárik, Rev. Sci. Instrum. **85**, 103507 (2014).
22. P. W. Bradford, N. C. Woolsey, G. G. Scott, G. Liao, H. Liu, Y. Zhang, B. Zhu, C. Armstrong, S. Astbury, C. Brenner, P. Brummitt, F. Consoli, I. East, R. Gray, D. Haddock, P. Huggard, P. J. R. Jones, E. Montgomery, I. Musgrave, P. Oliveira, D. R. Rusby, C. Spindloe, B. Summers, E. Zemaityte, Z. Zhang, Y. Li, P. McKenna, and D. Neely, High Power Laser Sci. Eng. **6**, e21 (2018).
23. J. L. Dubois, P. Raczka, S. Hulin, M. Rosiński, L. Ryć, P. Parys, A. Zaraś-Szydłowska, D. Makaruk, P. Tchórz, J. Badziak, J. Wołowski, J. Ribolzi, and V. T. Tikhonchuk, Rev. Sci. Instrum. **89**, 103301 (2018).
24. S. Kar, H. Ahmed, G. Nersisyan, S. Brauckmann, F. Hanton, A. L. Giesecke, K. Naughton, O. Willi, C. L. S. Lewis, and M. Borghesi, Phys. Plasmas **23**, 055711 (2016).
25. M. Bardon, J. G. Moreau, L. Romagnani, C. Rousseaux, M. Ferri, F. Lefévre, I. Lantuéjoul, B. E. Bazzoli, and D. Farcage, Plasma Phys. Control. Fusion **62**, 125019 (2020).
26. Y. Yan, T. Jiang, J. Chen, X. Liu, L. Meng, Z. Cheng, and Z. Liu, Rev. Sci. Instrum. **89**, 074703 (2018).
27. V. I. Koshelev, Y. I. Buyanov, B. M. Koval'chuk, Y. A. Andreev, V. P. Belichenko, A. M. Efremov, V. V. Plisko, K. N. Sukhushin, V. A. Vizir, V. B. Zorin, Proc. SPIE **3158**, 209 (1997).
28. S.-H. Min, H. Jung, O. Kwon, M. Sattorov, S. Kim, S.-H. Park, D. Hong, S. Kim, C. Park, B. H. Hong, I. Cho, S. Ma, M. Kim,

Y. J. Yoo, S. Y. Park, and G.-S. Park, IEEE Access **9**, 136775 (2021).

29. K. H. Schoenbach, S. J. Hargrave, R. P. Joshi, J. F. Kolb, R. Nuccitelli, C. Osgood, A. Pakhomov, M. Stacey, R. J. Swanson, J. A. White, S. Xiao, J. Zhang, S. J. Beebe, P. F. Blackmore, and E. S. Buescher, IEEE Trans. Dielectric. Electric. Insulat. **14**, 1088 (2007).

30. A. Kiełbik, W. Szlasa, V. Novickij, A. Szewczyk, M. Maciejewska, J. Saczko, and J. Kulbacka, Sci. Rep. **11**, 15835 (2021).

31. M. Ehret, D. de Luis, J. I. Apiñaniz, J. L. Henares, R. Lera, J. A. Pérez-Hernández, P. Puyuelo-Valdes, L. Volpe, and G. Gatti, Plasma Phys. Control. Fusion **66**, 045003 (2024).

32. L. Volpe, R. Fedosejevs, G. Gatti, J. A. Pérez-Hernández, C. Méndez, J. Apiñaniz, X. Vaisseau, C. Salgado, M. Huault, S. Malko, G. Zeraouli, V. Ospina, A. Longman, D. De Luis, K. Li, O. Varela, E. García, I. Hernández, J. D. Pisonero, J. G. Ajates, J. M. Alvarez, C. García, M. Rico, D. Arana, J. Hernández-Toro, and L. Roso, High Power Laser Sci. Eng. **7**, e25 (2019).

33. M. Roth and M. Schollmeier, in *Proceedings of the CAS-CERN Accelerator School: Plasma Wake Acceleration* (2016), p. 231.

34. J. Derouillat, A. Beck, F. Pérez, T. Vinci, M. Chiaramello, A. Grassi, M. Flé, G. Bouchard, I. Plotnikov, N. Aunai, J. Dargent, C. Riconda, and M. Grech, Phys. Commun. **222**, 351 (2018).

35. Y. Ping, R. Shepherd, B. F. Lasinski, M. Tabak, H. Chen, H. K. Chung, K. B. Fournier, S. B. Hansen, A. Kemp, D. A. Liedahl, K. Widmann, S. C. Wilks, W. Rozmus, and M. Sherlock, Phys. Rev. Lett. **100**, 085004 (2008).

36. J. Yu, Z. Jiang, J. C. Kieffer, and A. Krol, Phys. Plasmas **6**, 1318 (1999).

37. M. H. Key, M. D. Cable, T. E. Cowan, K. G. Estabrook, B. A. Hammel, S. P. Hatchett, E. A. Henry, D. E. Hinkel, J. D. Kilkenny, J. A. Koch, W. L. Kruer, A. B. Langdon, B. F. Lasinski, R. W. Lee, B. J. MacGowan, A. MacKinnon, J. D. Moody, M. J. Moran, A. A. Offenberger, D. M. Pennington, M. D. Perry, T. J. Phillips, T. C. Sangster, M. S. Singh, M. A. Stoyer, M. Tabak, G. L. Tietbohl, M. Tsukamoto, K. Wharton, and S. C. Wilks, Phys. Plasmas **5**, 1966 (1998).

38. M. Passoni and M. Lontano, Phys. Rev. Lett. **101**, 115001 (2008).

39. S. C. Wilks, W. L. Kruer, M. Tabak, and A. B. Langdon, Phys. Rev. Lett. **69**, 1383 (1992).

40. C. Salgado-López, A. Curcio, G. Gatti, J. L. Henares, J. I. Apiñaniz, J. A. P. Pérez-Hernández, L. Volpe, and D. de Luis, in *Proceedings of the 11th International Beam Instrumentation Conference* (2022), p. 352.

41. S. Sakata, S. Lee, H. Morita, T. Johzaki, H. Sawada, Y. Iwasa, K. Matsuo, K. F. Farley Law, A. Yao, M. Hata, A. Sunahara, S. Kojima, Y. Abe, H. Kishimoto, A. Syuhada, T. Shiroto, A. Morace, A. Yogo, N. Iwata, M. Nakai, H. Sakagami, T. Ozaki, K. Yamanoi, T. Norimatsu, Y. Nakata, S. Tokita, N. Miyanaga, J. Kawanaka, H. Shiraga, K. Mima, H. Nishimura, M. Bailly-Grandvaux, J. J. Santos, H. Nagatomo, H. Azechi, R. Kodama, Y. Arikawa, Y. Sentoku, and S. Fujioka, Nat. Commun. **9**, 3937 (2018).

42. G. Pérez-Callejo, C. Vlachos, C. A. Walsh, R. Florido, M. Bailly-Grandvaux, X. Vaisseau, F. Suzuki-Vidal, C. McGuffey, F. N. Beg, P. Bradford, V. Ospina-Bohórquez, D. Batani, D. Raffestin, A. Colaïtis, V. Tikhonchuk, A. Casner, M. Koenig, B. Albertazzi, R. Fedosejevs, N. Woolsey, M. Ehret, A. Debayle, P. Loiseau, A. Calisti, S. Ferri, J. Honrubia, R. Kingham, R. C. Mancini, M. A. Gigosos, and J. J. Santos, Phys. Rev. E **106**, 035206 (2022).

43. C. A. Walsh, R. Florido, M. Bailly-Grandvaux, F. Suzuki-Vidal, J. P. Chittenden, A. J. Crilly, M. A. Gigosos, R. C. Mancini, G. Pérez-Callejo, C. Vlachos, C. McGuffey, F. N. Beg, and J. J. Santos, Plasma Phys. Control. Fusion **64**, 025007 (2022).

44. T. Shao, K. Long, C. Zhang, P. Yan, S. Zhang, and R. Pan, J. Phys. D **41**, 215203 (2008).

45. J. M. Sanders, A. Kuthi, P. T. Vernier, Y.-H. Wu, C. Jiang, and M. A. Gundersen, in *2009 IEEE Pulsed Power Conference* (2009), p. 1418.

46. T. B. Naptonik, M. Reberšek, P. T. Vernier, B. Mali, and D. Miklavčič, Bioelectrochemistry **110**, 1 (2016).

47. B. Greenebaum, Bioelectromagnetics **43**, 47 (2022).

48. A. Porcher, N. Wilmot, P. Bonnet, V. Procaccio, and A. Vian, Bioelectromagnetics **45**, 4 (2023).

49. R. Fabbro, C. Max, and E. Fabre, Phys. Fluids **28**, 1463 (1985).

50. F. N. Beg, A. R. Bell, A. E. Dangor, C. N. Danson, A. P. Fews, M. E. Glinsky, B. A. Hammel, P. Lee, P. A. Norreys, and M. Tatarakis, Phys. Plasmas **4**, 447 (1997).

51. A. Poyé, J.-L. Dubois, F. Lubrano-Lavaderci, E. D'Humières, M. Bardon, S. Hulin, M. Bailly-Grandvaux, J. Ribolzi, D. Raffestin, J. J. Santos, P. Nicolaï, and V. Tikhonchuk, Phys. Rev. E **92**, 043107 (2015).

52. https://www.scayle.es.